





Statistical Study of Ion Upflow and Downflow Observed by PFISR

Jiaen Ren¹ , Shasha Zou¹ , Jiayue Lu², Naomi Giertych³, Yang Chen³ , Roger H. Varney⁴ , and Ashton S. Reimer⁴ 

¹Department of Climate and Space Sciences and Engineering, College of Engineering, University of Michigan, Ann Arbor, MI, USA, ²Department of Computer Science, College of Literature, Science, and the Arts, University of Michigan, Ann Arbor, MI, USA, ³Department of Statistics, College of Literature, Science, and the Arts, University of Michigan, Ann Arbor, MI, USA, ⁴Center for Geospace Studies, SRI International, Menlo Park, CA, USA

Key Points:

- The occurrence frequency of ion upflow increases with enhanced geomagnetic activity level and stronger solar wind and IMF driving
- Ion upflow at PFISR latitude is twice more likely to occur on the nightside than on the dayside
- Peak ion downflow occurrence rate reaches 30% on the dayside during strongly positive IMF B_y and negative B_z , associated with SED and plume

Supporting Information:

- Supporting Information S1

Correspondence to:

J. Ren,
jiaenren@umich.edu

Citation:

Ren, J., Zou, S., Lu, J., Giertych, N., Chen, Y., Varney, R. H., & Reimer, A. S. (2020). Statistical study of ion upflow and downflow observed by PFISR. *Journal of Geophysical Research: Space Physics*, 125, e2020JA028179. <https://doi.org/10.1029/2020JA028179>

Received 29 APR 2020

Accepted 2 OCT 2020

Accepted article online 10 OCT 2020

Abstract Ion upflow in the F region and topside ionosphere can greatly influence the ion density and fluxes at higher altitudes and thus has significant impact on ion outflow. We investigated the statistical characteristics of ion upflow and downflow using a 3-year (2011–2013) data set from the Poker Flat Incoherent Scatter Radar (PFISR). Ion upflow is twice more likely to occur on the nightside than on the dayside in PFISR observations, while downflow events occur more often in the afternoon sector. Upflow and downflow on the dayside tend to occur at altitudes ~ 500 km, higher than those on the nightside. Both upflow and downflow occur more frequently as ion convection speed increases. Upflow observed from 16 to 6 magnetic local time through midnight is associated with temperature and density enhancements. Occurrence rates of upflow on the nightside and downflow on the dayside increase with geomagnetic activity level. On the nightside, occurrence rate of ion upflow increases with enhanced solar wind and interplanetary magnetic field (IMF) drivers as well as southwestward local magnetic perturbations. The lack of correlation of upflow on the dayside with the solar wind and IMF parameters is because PFISR is usually equatorward of the dayside auroral zone. Occurrence rate of downflow does not show strong dependence on the solar wind and IMF conditions. However, it occurs much more frequently on the dayside when the IMF $B_y > 10$ nT and the IMF $B_z < -10$ nT, which we suggest is associated with the decaying of the dayside storm-enhanced density (SED) and the SED plume.

1. Introduction

Over the last three decades, numerous studies have shown that ionospheric ions not only can get into the magnetosphere but also contribute as an important source of magnetospheric plasma (e.g., Chappell, 2015; Lotko, 2007; Moore & Horwitz, 2007; Welling et al., 2015; Yau & Andre, 1997, and references therein). Ion upflow events in the F region and topside ionosphere can greatly influence the ion density and fluxes at further higher altitudes, and thus controls to a great extent directly the ion outflow fluxes observed at high altitudes (e.g., Nilsson et al., 2008; Strangeway, 2005; Tu et al., 2007).

Observational characterization of the ion upflow occurrence rate can provide valuable information about the available source population as a function of solar wind and interplanetary magnetic field (IMF) condition, as well as the level of geomagnetic activity. Ion upflow and downflow events occurring in the F region and topside ionosphere have been studied using data from ground-based incoherent scatter radars (ISRs) (e.g., Buchert et al., 2004; Endo et al., 1999; Foster et al., 1998; Ji et al., 2019; Keating et al., 1990; Liu et al., 2001; Ogawa et al., 2009; Semeter et al., 2003; Zou, Ozturk, et al., 2017; Zou, Ridley, et al., 2017) and in situ satellite observations (Coley et al., 2006; Loranc et al., 1991; Redmon et al., 2010; Seo et al., 1997; Wu et al., 2000). The in situ satellite observations have large spatial coverage but limited coverage of altitude at any given time; while the ground-based ISRs, which are at fixed geographic locations, are able to provide altitude profiles of important plasma state parameters that can shed light on their formation mechanisms. In addition, some of the satellite observations mentioned above actually measure the vertical flows, while the ground-based ISRs can measure the field-aligned flows as well as the vertical flows.

The observed ion upflow exhibits considerable spatial and temporal variations. Based on satellite observations, the occurrence rate of upflow is generally larger than that of downflow in the auroral zone, but smaller in the polar cap. The downflow in the polar cap was observed using the DE-2 satellite and suggested to

be ballistic return of outflowing ions (Loranc et al., 1991), which was later studied using simulations (Loranc & St.-Maurice, 1994). Statistical studies of ion upflow are mainly conducted using the EISCAT radars at either Tromso (Endo et al., 1999; Foster et al., 1998; Keating et al., 1990) or Longyearbyen (Ji et al., 2019; Liu et al., 2001; Ogawa et al., 2009, 2019). The peak upflow occurrence rate is found in the pre-midnight sector near the Harang reversal region by EISCAT at Tromso, while on the dayside at EISCAT Longyearbyen. The difference is due to the different geomagnetic latitudes (MLat) of EISCAT Longyearbyen at ~ 75.4 MLat and EISCAT Tromso at ~ 66.7 MLat. This effect of MLat difference will be discussed in detail in section 4.

Despite that there was some first field-aligned ion upflow observations from the Chatanika ISR in Alaska (Bates, 1974), a comprehensive statistical study of upflow and downflow does not exist for the American sector. Under the simplest assumption, that is, neglecting the heat flow from the top of the ionosphere, the field-aligned component of the ionospheric ion velocity is affected by both the thermospheric wind and other vertical forces, including pressure gradient force and gravity. The magnetic field geometry affects the effectiveness of these forces, and the geomagnetic latitude determines the corresponding magnetospheric region, where the upflow and downflow map magnetically. Therefore, it is important to determine the geographical differences of occurrence rate of ion upflow and downflow, and test their dependence on season, IMF, and solar wind, as well as geomagnetic activity. To fill the gap, in this study, we use the Poker Flat ISR (PFISR) to conduct such a statistical study of the occurrence rate of upflow and downflow in the American sector.

In addition, unlike the traditional ISRs, PFISR is part of the Advanced Modular ISR (AMISR) system with electronic pulse-to-pulse steering capability, which allows nearly simultaneous measurements of the plasma parameters in multiple look directions without physical movement of the radar antenna. Moreover, while ISRs are generally expensive to run, PFISR can operate semicontinuously in a low-duty cycle mode between user-requested high-duty cycle experiments, providing a better data coverage throughout the year. Therefore, there are far more field-aligned profiles available from PFISR than those from other traditional ISRs for statistical analysis.

In the next section, the methodology used to identify the ion upflow and downflow events is described. In section 3, statistical results regarding the density, temperature, fluxes, and occurrence rates of ion upflow and downflow as a function of season, magnetic local time (MLT), ionosphere convection, local magnetic perturbation, geomagnetic activity level, and solar wind and IMF are presented. Summary of the findings of this study is given in section 4.

2. Methodology

The PFISR radar is part of the NSF-supported AMISR facility that is used to conduct studies of the upper atmosphere and to observe space weather events. The PFISR data used in this study are downloaded from the SRI AMISR database and the CEDAR Madrigal database. Considering the solar cycle trend and gradual decay of the radar transmit power over time, PFISR has some of its highest quality data from 2011 to 2013 during the peak of solar cycle 24. Therefore, we selected these 3 years (2011–2013) of PFISR data to conduct the statistical study.

2.1. Upflow and Downflow Event Identification

The field-aligned ion velocity profiles from the long-pulse PFISR data are used to identify the ion upflow and downflow events. In the high-altitude ionosphere, the ISR data might have large measurement uncertainties. Therefore, we select our upflow and downflow events based on the following criteria. First, we have data quality control criteria that the ratio between the velocity measurement uncertainty and the magnitude of the measurement itself must be smaller than one unless the uncertainty is less than 100 m/s. Second, following the method used in Ogawa et al. (2009), we select reliable ion upflow/downflow events when there are at least three consecutive ion field-aligned speed larger/smaller than 100/–100 m/s in the velocity altitude profile. Figure 1 shows examples of the identified ion upflow events (left) and downflow events (right). Dots with green crosses indicate data points satisfying the defined upflow/downflow events selection criteria, while dots with red crosses mean low-quality data points that fail to meet the first criterion. As a result, a total of 36,061 upflow events (or vertical profiles) and 39,632 downflow events (or vertical profiles) have been

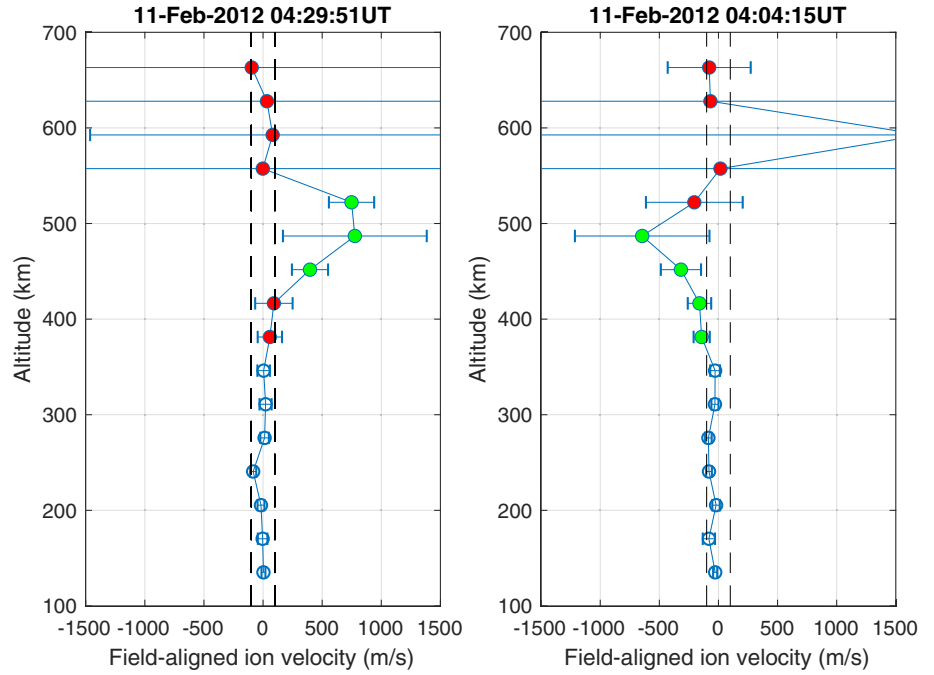


Figure 1. Examples of identified ion upflow and downflow events. The left and right panels show examples of an ion upflow record and a downflow record, respectively, on 11 February 2012. The dashed vertical lines mark $-100/100$ m/s field-aligned ion velocity. The dots in red mark the invalid data points that do not satisfy the data quality criteria, while those in green indicate all the valid data points with velocity smaller/larger than $-100/100$ m/s for downflow/upflow. Profiles with at least three consecutive green dots are selected as downflow/upflow events.

identified in these 3-year data. A more restrict data selection method has also been used and the results are similar and included in the supporting information.

2.2. Occurrence Rate Estimation

The identified upflow and downflow data sets are then binned according to MLT, month, geomagnetic activity level indicated by the SymH index, and the auroral electrojet index (AE), as well as solar wind and IMF conditions. For each bin the relative occurrence rate of ion upflow and downflow is defined by

$$f(X) = \frac{n(X)}{N(X)} \quad (1)$$

where the variable X could be MLT, month, AE, SymH, solar wind, or IMF parameters, the numerator n is the number of upflow and downflow events in the bin, and the denominator N is the total number of PFISR observations available in that bin. To illustrate more robust statistics, we only show bins with N larger than 20. In order to estimate the uncertainty of the occurrence frequency, we use the following formula to calculate the standard deviation σ within each bin:

$$\sigma = \sqrt{\frac{f^*(1-f)}{N-1}} \quad (2)$$

where f is the frequency. Depending on the integration time, the PFISR data have 1- to 5-min time resolutions. The range resolution is 36 and 24 km for 480 and 330 μ s pulse length, respectively, which is comparable to the data used in Ogawa et al. (2009). To associate geomagnetic indices such as the SymH, AE, as well as solar wind and IMF data with each PFISR measurement record, we calculated the average values of these data within a 5-min window before the center of the measurement time and matched them with each measurement record.

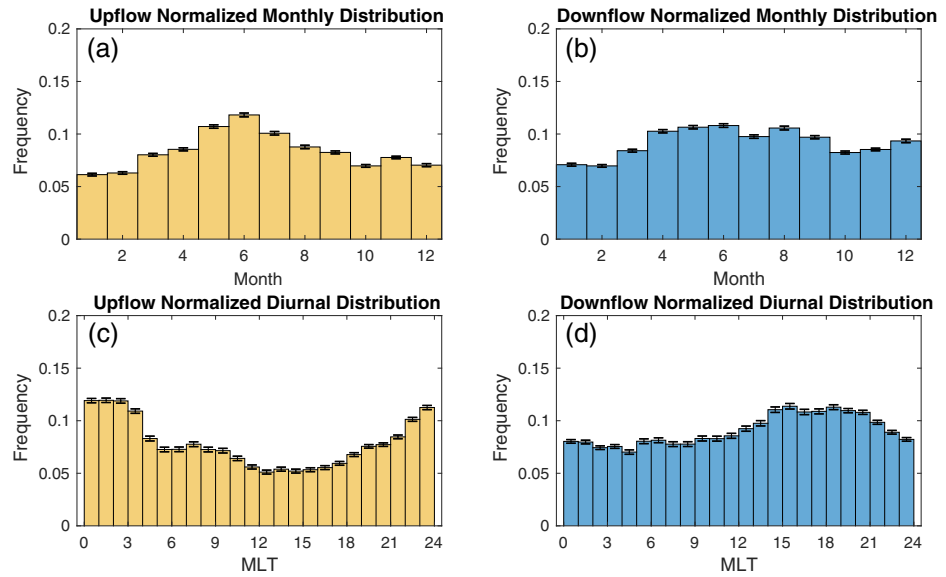


Figure 2. Monthly distribution of ion (a) upflow and (b) downflow occurrence frequencies. Magnetic local time (MLT) distribution of ion (c) upflow and (d) downflow occurrence frequencies. MLT is universal time (UT) + 13 at the PFISR site.

3. Results

3.1. Diurnal and Seasonal Variations of Ion Upflow and Downflow Altitude and Occurrence Frequency

The left panels in Figure 2 show the distribution of ion upflow occurrence frequency over months (top panels) and MLT (bottom panels). MLT is roughly UT + 13 hr at PFISR located near Fairbanks, Alaska. In the seasonal plots (top panels), the upflow and downflow occurrence frequencies reach the maximum (~12%) near-summer solstice, that is, May–July, and the minimum (~6%) after winter solstice, that is, January–February. (Figures 2a and 2b).

In Figures 2c and 2d, ion upflow occurs more often on the nightside centered just after midnight, that is, 23–3 MLT. The upflow occurrence frequency reaches the maximum (~12%) around midnight, which is more than double the minimum occurrence rate (~5%) in the noon sector (Figure 2c). In contrast, the downflow occurs more often in the dusk sector. The downflow occurrence frequency reaches the maximum (~11.3%) in the dusk sector, while the minimum (~7%) occurs just before dawn (Figure 2d).

The distributions of altitudes of the upflow and downflow as a function of MLT are shown in Figure 3. On the nightside, both upflow and downflow tend to occur around 400 km, while on the dayside the altitude increases to slightly above/below 500 km for upflow/downflow.

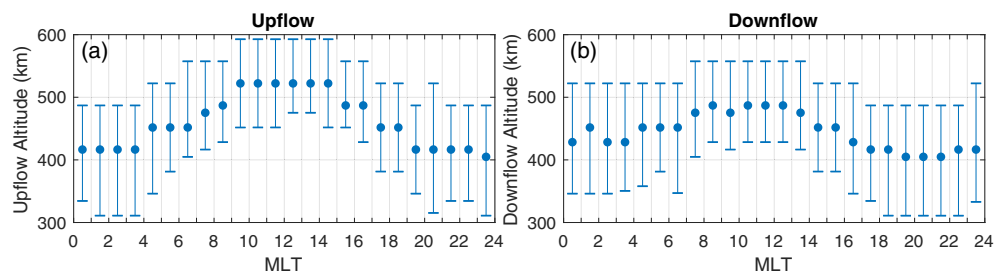


Figure 3. Median altitudes of ion (a) upflow and (b) downflow observed by PFISR at each MLT. The dots mark the median altitude of upflow/downflow observed within each MLT bin, while the vertical bars indicate the interquartile range from 25% to 75%.

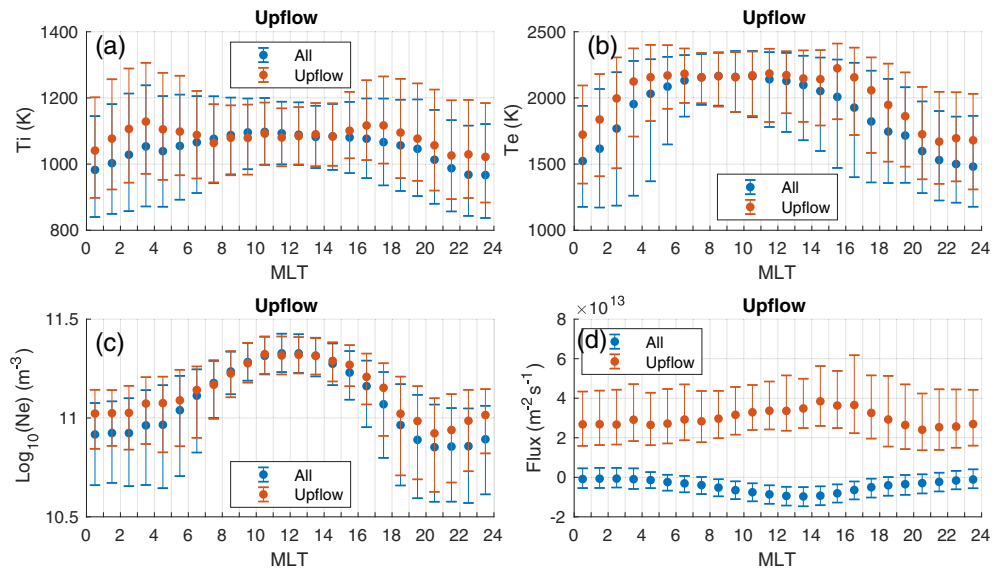


Figure 4. Distribution of (a) ion and (b) electron temperature, (c) electron density, and (d) field-aligned ion flux, averaged below 600 km, as a function of MLT with only ion upflow profiles and with all the profiles. The upflow flux is averaged over altitudes where the upflow occurs. The dots mark the median value for each bin and the vertical bars indicate the interquartile range from 25% to 75%.

3.2. Ionosphere Density, Temperature, and Field-Aligned Flux Associated With Ion Upflow and Downflow

Figures 4 and 5 show distributions of ion and electron temperature as well as density and flux, averaged below 600-km altitude, as a function of MLT with only ion upflow/downflow profiles and also with all the profiles for comparison. On the dayside, due to solar radiation, the overall median electron temperature is ~2200 K, 700 K higher than that on the nightside (Figure 4b), and the overall median electron density is $\sim 10^{11.3} \text{ m}^{-3}$, about 2.5 times the density near midnight (Figure 4c). The median fluxes for ion upflow are

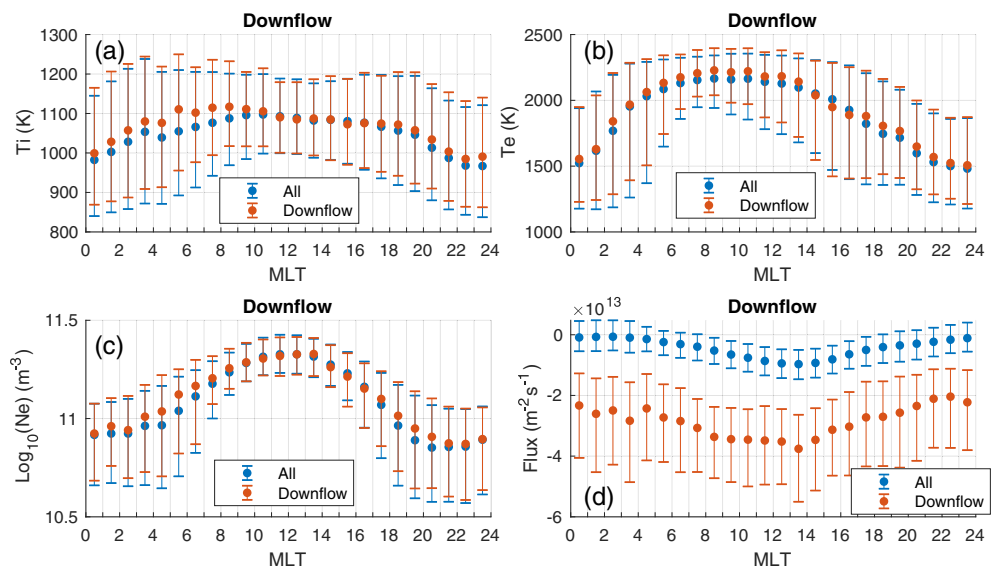


Figure 5. Distribution of (a) ion and (b) electron temperature, (c) electron density, and (d) field-aligned ion flux, averaged below 600 km, as a function of MLT with only ion downflow profiles and with all the profiles. The downflow flux is averaged over altitudes where the downflow occurs. The dots mark the median value for each bin and the vertical bars indicate the interquartile range from 25% to 75%.

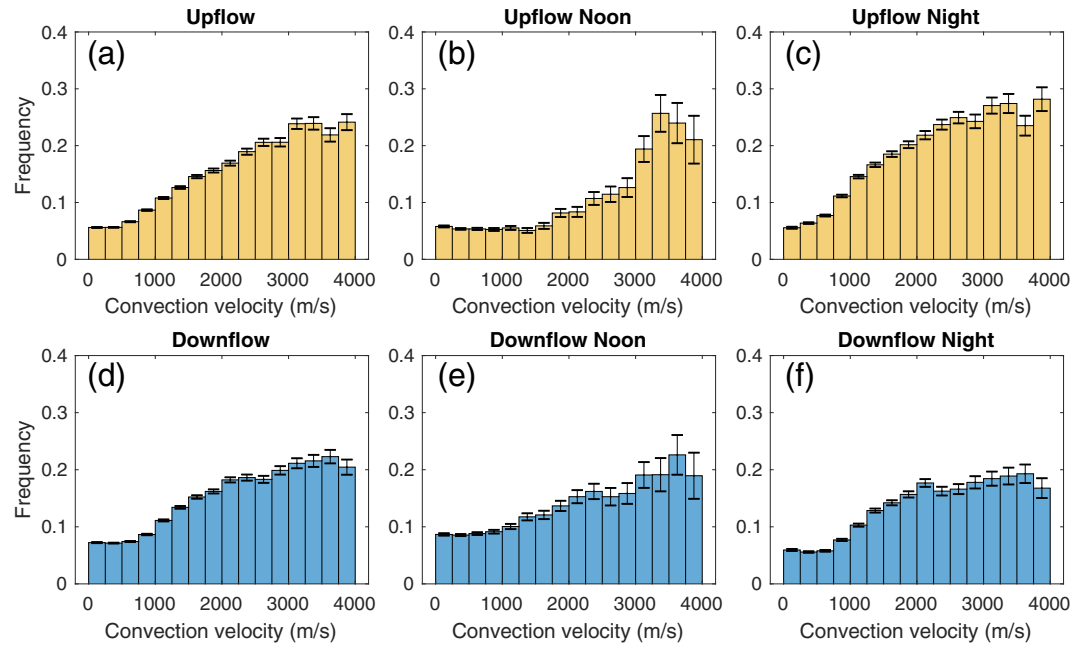


Figure 6. Occurrence frequency of ion upflow and downflow as a function of ion convection velocity for different MLT intervals: (a) all MLTs, (b) on the dayside between 9–15 MLT (4,831 upflow, 7,667 downflow), (c) on the nightside between 21–3 MLT (15,911 upflow, 12,292 downflow). (d–f) Downflow occurrence frequencies are in the same format as that for upflow.

$\sim 3 \times 10^{13} \text{ m}^{-2} \text{ s}^{-1}$ and are slightly larger during daytime due to the higher density (Figure 4d). There are clear electron ($\sim 200 \text{ K}$) and ion ($\sim 50 \text{ K}$) temperature enhancements for upflow observed from 16 to 6 MLT throughout the nightside, which suggests that ion upflow seen at those MLTs is more likely associated with auroral particle precipitations.

For ion downflow, as shown in Figure 5, there is no clear difference in temperature or density comparing with the overall values at each MLT, except that near $\sim 6 \text{ MLT}$ the downflow is associated with an $\sim 50 \text{ K}$ increase in the median ion temperature. The median fluxes of downflow vary between 2 and $4 \times 10^{13} \text{ m}^{-2} \text{ s}^{-1}$, depending on the MLT.

3.3. Local Ion Convection Speed Dependence of the Ion Upflow and Downflow Occurrence Frequency

Ion convection speed (averaged from 65.25 to 66 MLat) derived from PFISR multiple-beam line-of-sight ion velocity measurements were matched with each PFISR altitude profile, and its correlation with upflow/downflow occurrence frequency is shown in Figure 6. Overall, the occurrence frequency of both upflow and downflow increases almost monotonically as convection velocity increases, and the upflow occurrence is more sensitive to the convection flow speed as indicated by the slope of the trend. For upflow on the dayside, the occurrence frequency stays below 10% until convection speed exceeds 2.5 km/s, where the frequency jumps to $\sim 20\%$, whereas on the nightside, the frequency grows rapidly as convection velocity exceeds as low as 750 m/s and reaches 20% at $\sim 1.5 \text{ km/s}$.

This strong correlation between the upflow occurrence and convection flow speed is consistent with the theory that the frictional heating caused by enhanced convection can lead to ion upflow (Ma et al., 2018; Strangeway, 2005; Zhang et al., 2016). The higher increasing rate on the nightside is likely due to the fact that convection flows and particle precipitations tend to occur at the same time around midnight during enhanced geomagnetic disturbances, and the enhanced convection flows can extend to latitudes lower than the auroral precipitation boundary but the separation between the two boundaries are narrower on the nightside (Zou, Lyons, Wang, et al., 2009; Zou, Lyons, Nicolls, et al., 2009).

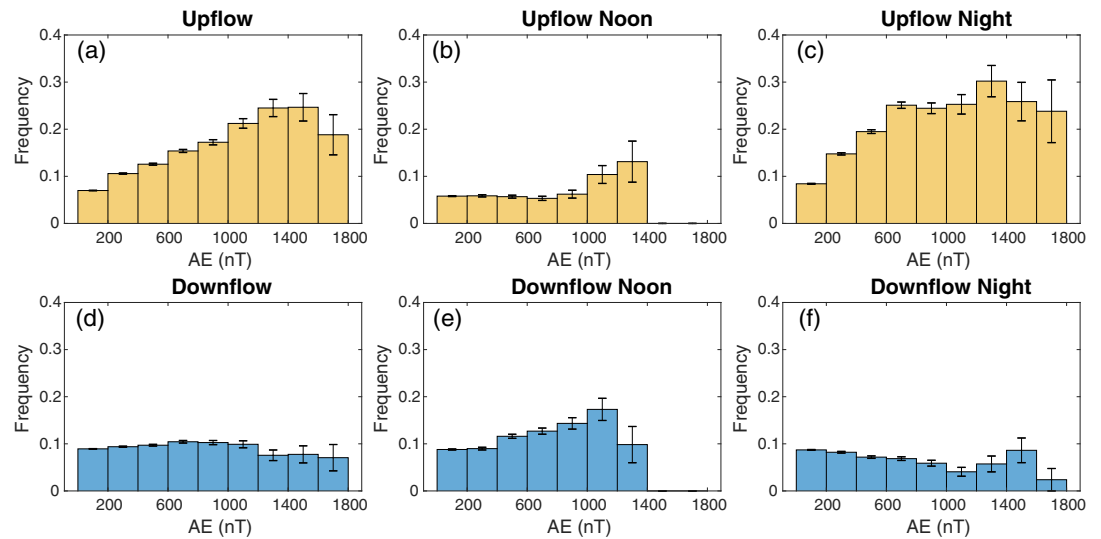


Figure 7. Ion upflow (first row) occurrence frequency plotted over AE index over different MLT intervals: (a) all MLTs, (b) on the dayside between 9–15 MLT (4,831 upflow, 7,667 downflow), (c) on the nightside between 21–3 MLT (15,911 upflow, 12,292 downflow). (d–f) Downflow occurrence frequencies (second row) are in the same formats as those for the upflows.

3.4. Geomagnetic Activity Dependence of the Ion Upflow and Downflow Occurrence Frequency

3.4.1. AE Dependence

Figure 7 shows how the occurrence frequencies of ion upflow (top panels) and downflow (bottom panels) are influenced by the auroral electrojet strength represented by the AE index. From left to right, the two panels in the same column show occurrence frequencies averaged over all MLTs, only on the dayside (9–15 MLT) and only on the nightside (21–3 MLT), respectively. The occurrence rate of ion upflow averaged over all MLT (Figure 7a) increases steadily with AE from ~6% to ~25%. Although when AE is larger than 1,600 nT, the upflow occurrence frequency started to decrease as AE increases. This is likely due to the limited available number of events with AE higher than 1,600 nT, as evidenced by the increasing size of the error bar. On the

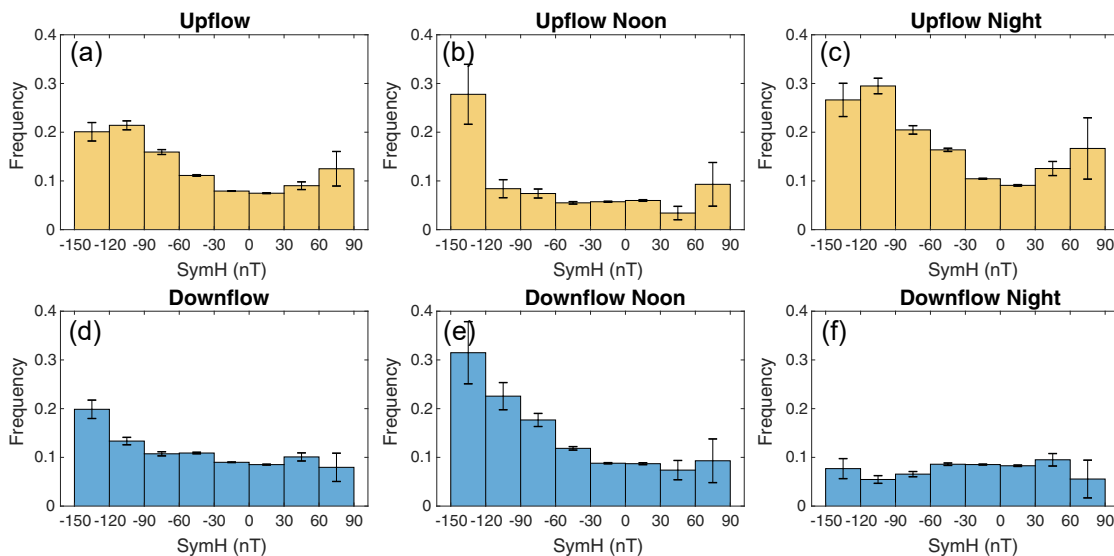


Figure 8. Ion upflow (first row) occurrence frequency plotted over SymH index over different MLT intervals: (a) all MLTs, (b) on the dayside between 9–15 MLT (4,831 upflow, 7,667 downflow), (c) on the nightside between 21–3 MLT (15,911 upflow, 12,292 downflow). (d–f) Downflow occurrence frequency (second row) formats the same as upflow.

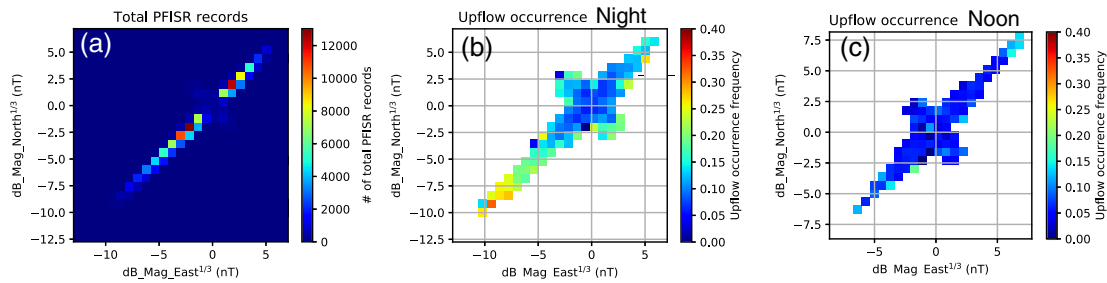


Figure 9. Heatmaps showing (a) distributions of local magnetic perturbations matched with all PFISR records, (b and c) distribution of ion upflow occurrence frequency on local magnetic perturbations for data on the (b) nightside between 21–3 MLT and (c) on the dayside between 9–15 MLT. The magnetic perturbations are measured in local magnetic north and east directions and are plotted after applying cubic root for better visual clarity.

dayside (Figure 7b), there is no obvious relationship between AE and the upflow occurrence rate for AE less than $\sim 1,000$ nT, where the rate is $\sim 5\%$. When AE is greater than 1,000 nT, the upflow occurrence rate on the dayside increases to $\sim 13\%$. On the nightside (Figure 7c), there is a clear increasing trend for the upflow occurrence rate, that is, from less than 10% for quiet time to $\sim 25\%$ when AE increases from 0 to ~ 700 nT. After AE exceeds ~ 700 nT, the upflow occurrence rate does not change significantly, while at the same time, the uncertainties reflected by the size of the error bar also increase after that due to the lack of observations.

The downflow occurrence frequency does not show any clear dependence with AE when averaged over all MLTs (Figure 7d), but it is positively correlated with AE on the dayside (Figure 7e) with the maximum occurrence rate of $\sim 17\%$ and weakly negatively correlated on the nightside (Figure 7f) with the peak occurrence rate of $\sim 9\%$ when AE is less than 300 nT. The negative correlation on the nightside becomes less obvious when AE increases to 1,000 nT due to the reduced availability of large AE events.

3.4.2. SymH Dependence

The dependence of ion upflow (top panels) and downflow (bottom panels) occurrence frequencies on the ring current strength represented by the SymH index is shown in Figure 8. From left to right, the three panels show occurrence rates averaged over all MLTs, in the dayside sector (09–15 MLT) and in the nightside sector (21–03 MLT), respectively. A clear increasing trend of the ion upflow occurrence rate with increasing ring current strength, that is, decreasing SymH, can be seen in Figure 8a. The upflow occurrence frequency increases from the minimum $\sim 7\%$ when SymH is ~ 15 nT to the maximum $\sim 21\%$ when SymH reaches ~ -100 nT. Interestingly, the upflow occurrence rate also increases when the SymH becomes strongly positive, that is, under conditions with strong compression of the magnetosphere. Similar to the dependence on the AE index, the dayside ion upflow occurrence frequencies show no obvious trend with SymH (Figure 8b) except for a significant increase when SymH reaches -120 nT. Under those strong driving conditions, the dayside auroral oval likely extends to much lower latitudes and engulfs PFISR. Thus, PFISR is able to probe the dayside auroral oval under these circumstances. A strong correlation between the nightside ion upflow occurrence rate and SymH can be seen in Figure 8c. The nightside occurrence of ion upflow increases with decreasing SymH down to ~ -120 nT reaching the maximum of about 29.5%. Again, the error bars are slightly larger for the large negative SymH events because of fewer PFISR measurements during such disturbed periods.

The ion downflow occurrence rate over all MLTs (Figure 8d) shows a weak increasing trend with decreasing SymH, due to exact opposite trends on the dayside (Figure 8e) and nightside (Figure 8f). On the dayside, there is a strong positive correlation between the downflow occurrence rate and the ring current strength, with the peak rate reaching $\sim 31\%$ at SymH ~ -135 nT. In contrast, the nightside occurrence rate of downflow (Figure 8f) shows no clear trend for quiet times (SymH ~ 0), but decreases slightly for large negative SymH.

3.4.3. Local Magnetic Perturbation Dependence

Comparing with global geomagnetic indices, local magnetic perturbation is likely a more sensitive indicator for local ion upflow activities. To study this, we used SuperMAG magnetic perturbation data with 1-min resolution and baseline subtracted (Gjerloev, 2012) at Poker Flat (PKR) and College (CMO) Station, which were matched with all the PFISR records at the closest minute. Figure 9 shows the correlation between ion upflow occurrence frequency and local magnetic perturbations. The overall magnetic perturbations near PFISR

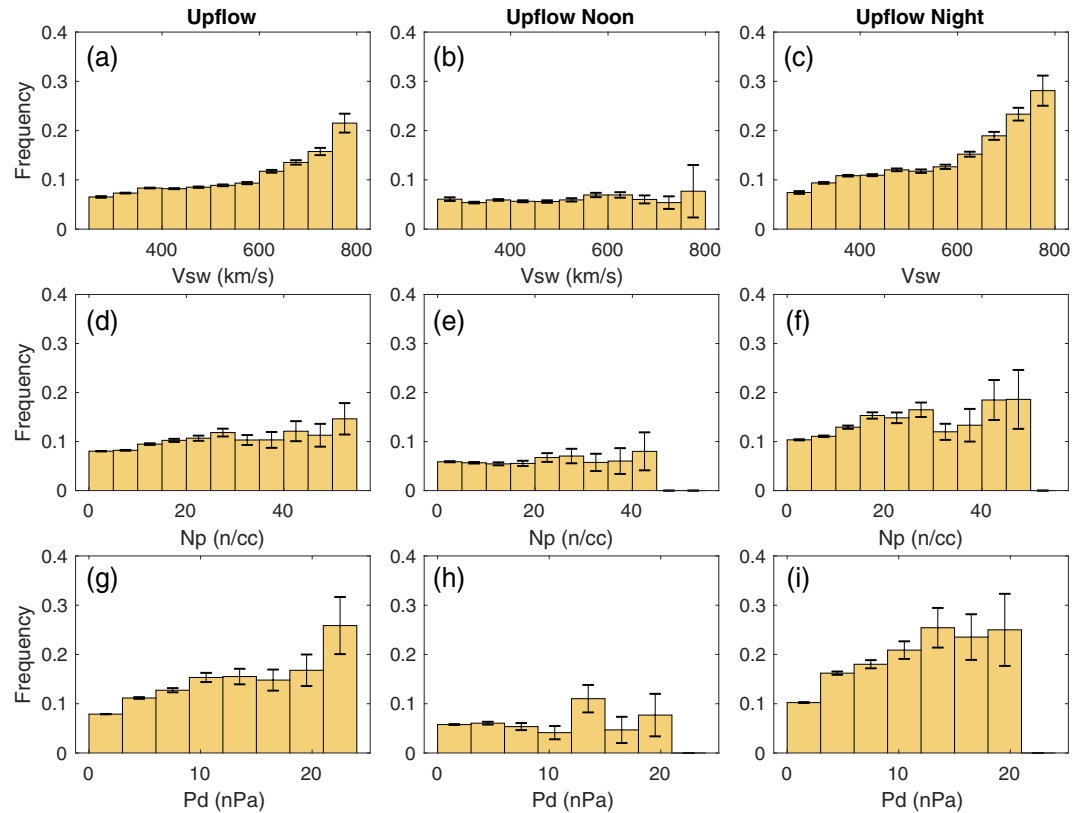


Figure 10. Ion upflow occurrence frequency plotted over solar wind parameters, extracted from NASA OMNI data set through OMNIWeb: Velocity (first row), proton number density (second row), dynamic pressure (third row), for different MLT intervals: (a, d, g) all MLTs, (b, e, h) on the dayside between 9–15 MLT (4,831 upflow, 7,667 downflow), (c, f, i) on the nightside between 21–3 MLT (15,911 upflow, 12,292 downflow).

(Figure 9a) are dominated by those in the southwestward and northeastward directions. On the nightside (Figure 9b), the occurrence frequency of ion upflow increases from below 10% with nearly no magnetic perturbation to above 25%, when there is strong southwestward magnetic perturbation reaching magnitude over 400 nT. The southwestward magnetic perturbation is due to a tilted westward electrojet typically seen just poleward of the Harang reversal (Zou, Lyons, Wang, et al., 2009). This clear correlation between the nightside ion upflow occurrence and the southwestward magnetic perturbation suggests that enhanced ion upflow occurrence is due to enhanced auroral precipitation associated with the substorms (Zou, Lyons, Wang, et al., 2009; Zou, Lyons, Nicolls, et al., 2009). Meanwhile, such correlation is not found on the dayside. For downflow occurrence (not shown here), no clear correlation is found on either dayside or nightside.

3.5. Solar Wind and IMF Dependence of Ion Upflow and Downflow Occurrence Rates

For solar wind and IMF parameters, extracted from NASA OMNI data set through OMNIWeb, we match them to the upflow/downflow data with the smallest time difference, then take the average of solar wind and IMF within 5 min ahead of the upflow or downflow events. Considering propagation of the IMF effects might take over 1 hr from bow shock nose to the nightside auroral zone (Browett et al., 2017; Rong et al., 2015; Zhang et al., 2015), alternative average durations up to 1 h r have been tested and no statistically significant differences in the results are found.

3.5.1. Solar Wind

Figure 10 shows how solar wind parameters (solar wind velocity (first row), proton number density (second row), and dynamic pressure (third row)) influence the occurrence frequencies of ion upflow. From left to right, the three panels in the same column show distributions over all MLTs, in the dayside sector and in

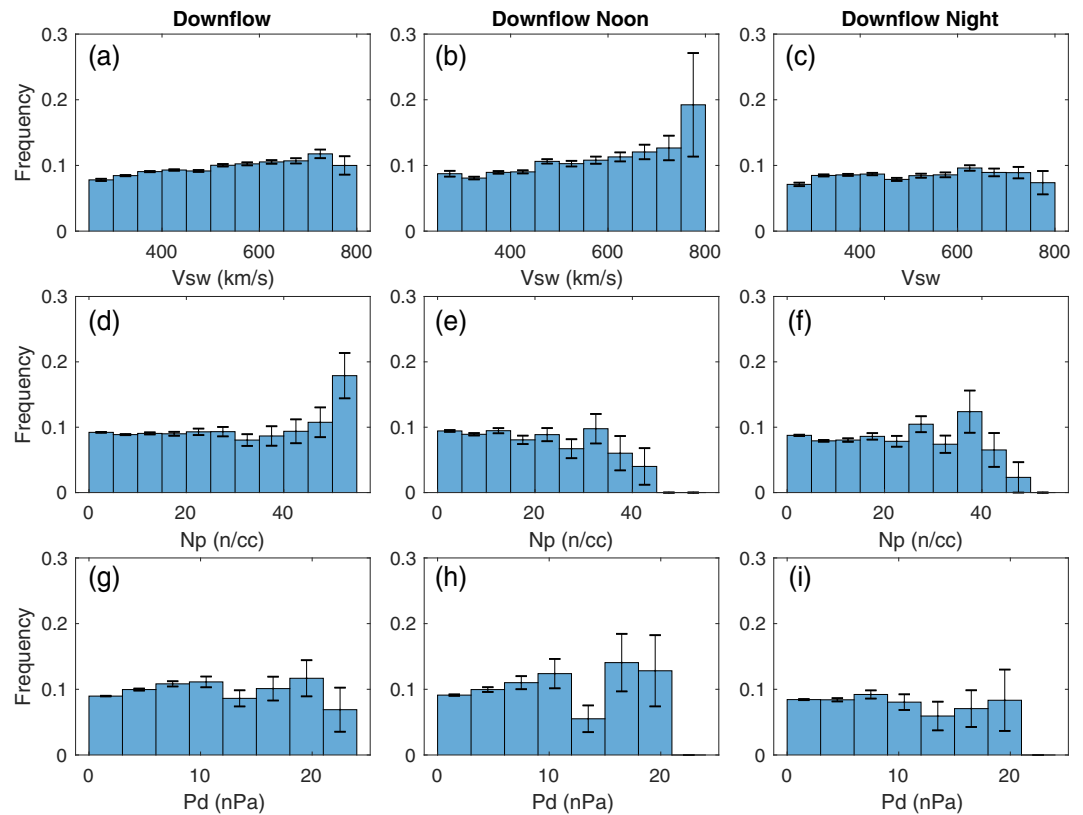


Figure 11. Ion downflow occurrence frequencies plotted over solar wind parameters, in the same format as ion upflow (Figure 10).

the nightside sector, respectively. The three panels in the first column show that the ion upflow occurrence rates slightly increase when the solar wind velocity, number density, and dynamic pressure increase in general. The solar wind velocity shows the strongest positive dependency with the upflow. In particular, the occurrence rate increases much faster for fast solar wind (>600 km/s) than that for slow solar wind speed. On the dayside (Figures 10b and 10e), no clear dependences appear between the solar wind velocity and proton number density and the ion upflow occurrence frequency. On the nightside (Figures 10c, 10f, and 10i), stronger dependences of the upflow occurrence rate on all three parameters can be observed, with the maximum occurrence frequency reaching $\sim 25\%$ during high solar wind velocity ~ 800 km/s or dynamic pressure ~ 20 nPa.

Similarly formatted as Figure 10, Figure 11 shows the dependence of the ion downflow occurrence frequencies on the solar wind velocity (top row), proton number density (middle row), and dynamic pressure (bottom row). The downflow occurrence frequency slightly increases as the velocity increases over all MLTs (Figure 11a) and in the dayside sector (Figure 11b). No clear dependence is observed between solar wind proton number density or dynamic pressure and the downflow occurrence, except that when the proton number density exceeds ~ 40 cm^{-3} , there is an increasing trend in the downflow occurrence frequency, with a peak of $\sim 18\%$ at ~ 55 cm^{-3} .

3.5.2. IMF

Figure 12 shows the dependence of ion upflow occurrence frequencies of the total IMF (first row), IMF B_x (second row), IMF B_y (third row), and IMF B_z (fourth row) in the Geocentric Solar Magnetospheric (GSM) coordinates. From left to right, the three columns of panels show distributions over all MLTs in the dayside sector and in the nightside sector, respectively. The overall upflow occurrence frequency in the dayside sector (Figures 12b, 12e, 12h, and 12k) is relatively low, that is, $\sim 10\%$, and insensitive to the IMF parameters. However, there are clear increasing trends between the ion upflow occurrence frequency and the total

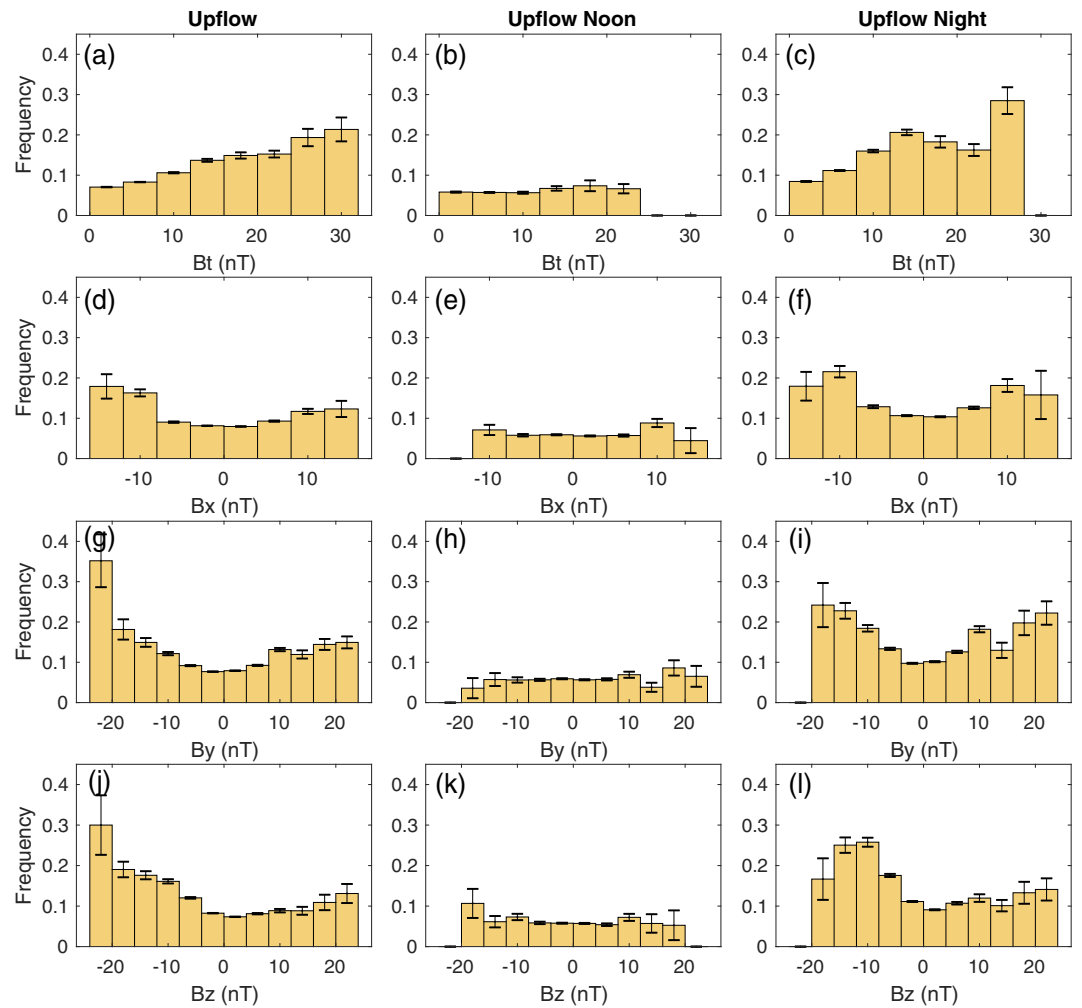


Figure 12. Ion upflow occurrence frequency plotted over the IMF components, extracted from NASA OMNI data set through OMNIWeb: Total IMF (first row), IMF B_x (second row), IMF B_y (third row), IMF B_z (fourth row), for different MLT intervals: (a, d, g) all MLTs, (b, e, h) on the dayside between 9–15 MLT (4,831 upflow, 7,667 downflow), (c, f, i) on the nightside between 21–3 MLT (15,911 upflow, 12,292 downflow).

IMF over all MLTs (Figure 12a) and in the nightside sector (Figure 12c). In Figures 7d, 7g, and 7j, a rough bimodal distribution with the center around zero can be observed for all three IMF components. The occurrence rate increases with the magnitude of the IMF components, and the maximum occurrence rate exceeds 17% for B_x near -12 nT and $>30\%$ for B_y and B_z below -20 nT. This bimodal distribution is even clearer in the nightside sector (Figures 12f, 12i, and 12l).

In the bottom row, the increasing trend of the upflow occurrence rate with negative B_z is much more rapid than that with positive B_z . It is very well known that strong energy coupling between the solar wind and the magnetosphere occurs when the IMF is southward (IMF $B_z < 0$). Therefore, as expected, the occurrence frequency of ion upflow increases with stronger geomagnetic activities and auroral zone expansions as the IMF B_z decreases. This increasing trend becomes less clear when the IMF B_z is strongly southward, that is, smaller than -12 nT, which again is likely due to the limited availability of strong southward IMF B_z events as evidenced by the larger error bars.

Figure 13 shows the dependence of the ion downflow occurrence frequencies of the total IMF (top row), IMF B_x (second row), IMF B_y (third row), and IMF B_z (bottom row). From left to right, the three columns of panels show distributions over all MLTs in the dayside sector and in the nightside sector, respectively. The overall correlation between the downflow occurrence frequency and the total IMF is positive, in particular on the

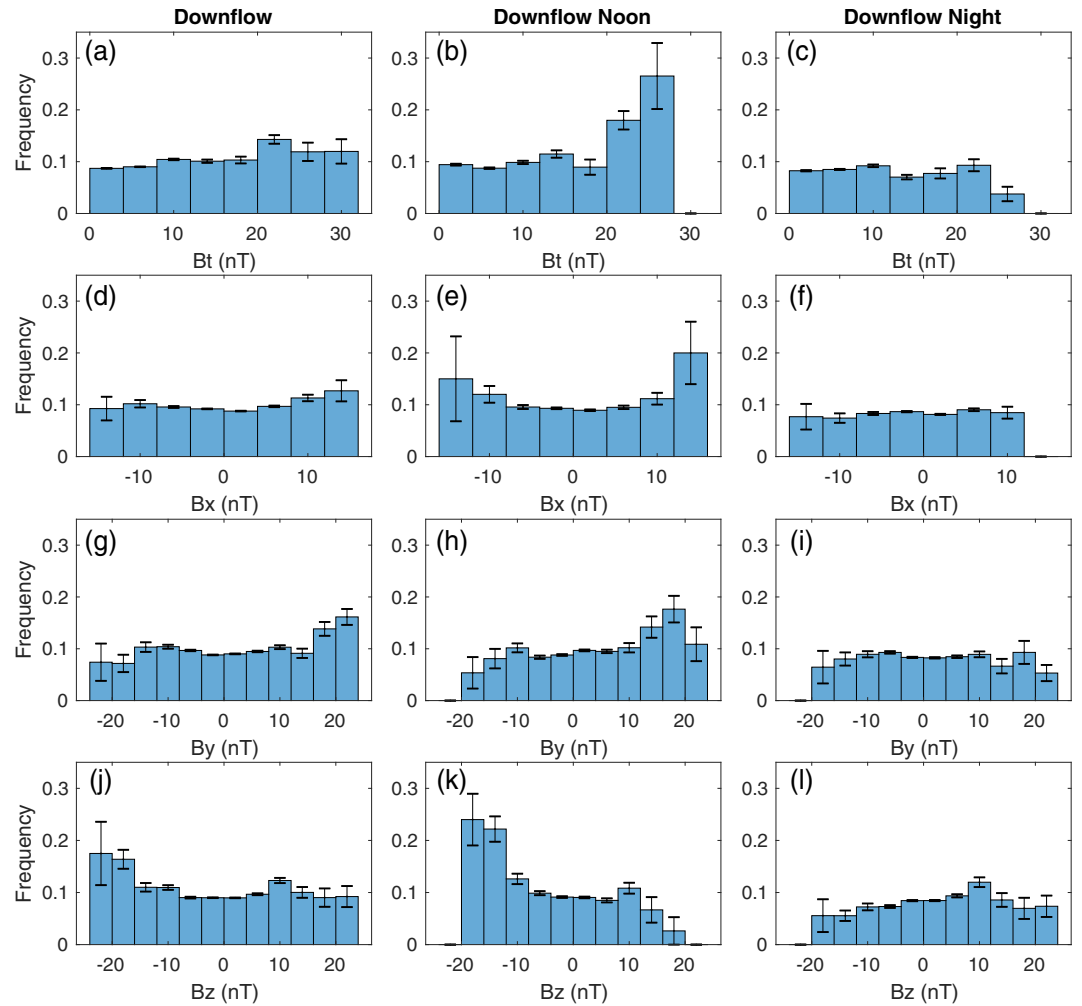


Figure 13. Ion downflow occurrence frequency plotted over the IMF components, with the same format as the ion upflow (Figure 12).

dayside (Figure 13b), while on the nightside there is no clear correlation (Figure 13c). No obvious dependency between the downflow occurrence frequency and B_x can be seen (Figures 13d–13f), except for extremely large $|B_x| > 12$ nT although the error bars become larger as well. In terms of B_y , on the dayside, the downflow clearly prefers to occur when B_y is strongly positive, and the maximum downflow occurrence frequency reaches $\sim 18\%$ when B_y is ~ 18 nT (Figure 13h). Similarly, in Figure 13k, the downflow occurrence frequency also prefers strongly negative B_z , that is, < -10 nT, on the dayside.

Since both the IMF B_y and B_z components have shown notable correlations with upflow/downflow occurrence frequency, joint distributions are shown in Figure 14 to further study the effects from the IMF clock angle and magnitude. Comparison between Figures 14e and 14h clearly indicates that, at Poker Flat, the upflow occurrence frequency is significantly higher on the nightside than it is on the dayside, at least when the IMF B_z is larger than -16 nT. Later discussion will suggest this is most likely due to its relative location with the auroral zone under quiet and moderate geomagnetic conditions. The overall occurrence of upflow, as shown in Figure 14b, increases as the IMF B_z decreases, and the highest occurrence frequencies are reached during strongly negative IMF B_z conditions when the IMF B_y also has magnitude larger than 8 nT. When the IMF B_z is near zero, the upflow occurrence shows a bimodal distribution on the IMF B_y , where the occurrence frequency increases as the IMF B_y increases its magnitude.

As for downflow, the highest occurrence frequencies are seen on the dayside when the IMF B_z is strongly negative ~ -14 nT and IMF B_y is strongly positive ~ 16 nT. Also, by comparing Figures 14f and 14i, it can

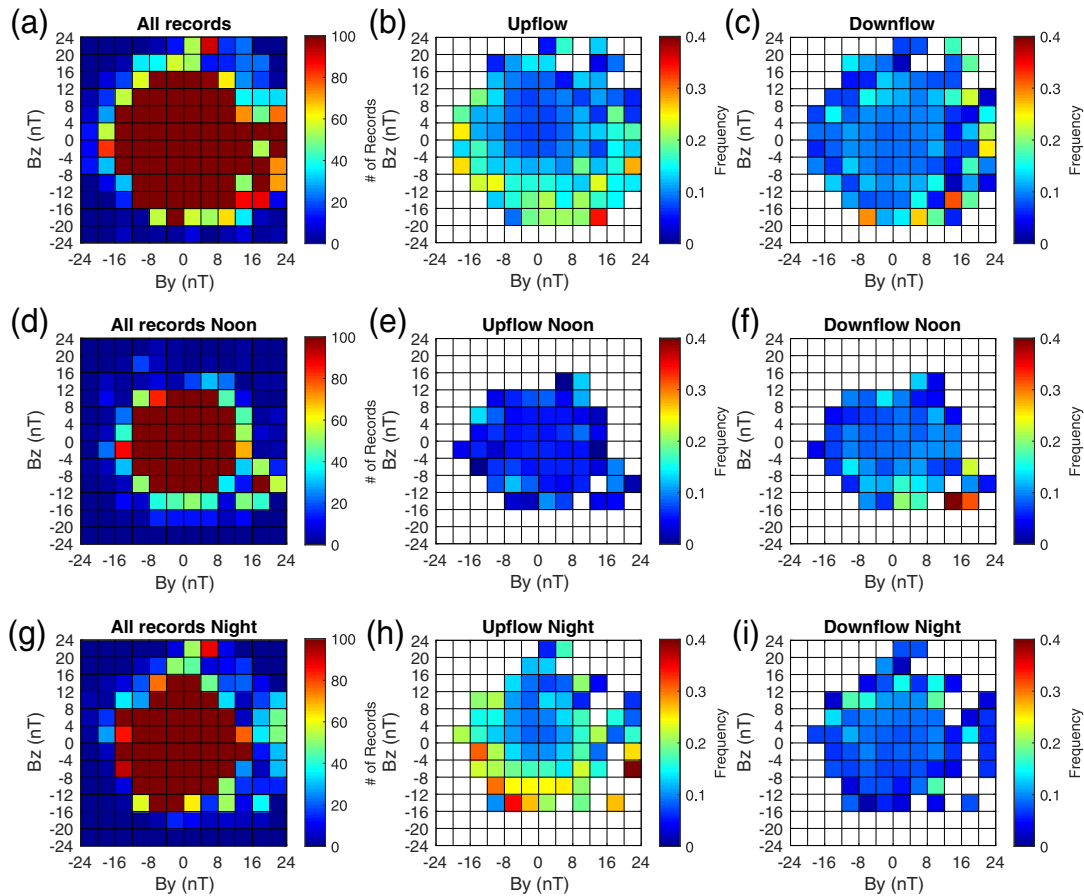


Figure 14. Heatmaps showing joint distributions of ion upflow/downflow occurrence frequency on the IMF B_y and IMF B_z components. Each row represents a certain MLT sector: (a–c) overall MLT (first row), (d–f) on the dayside between 9–15 MLT (second row), (g–i) on the night side between 21–3 MLT (third row). The first column indicates total count of records in each bin, while the second and third columns show distributions of upflow and downflow occurrence frequency, respectively.

be noticed that on the dayside negative IMF B_z conditions tend to favor the occurrence of downflow, while on the nightside downflow seems to occur more frequent during positive IMF B_z conditions.

4. Discussions

4.1. Upflow

It is generally known that ion upflow can be generated by either frictional heating mechanism (Type 1 upflow) or enhanced ambipolar electric field due to electron heating (Type 2 upflow) (Wahlund et al., 1992). These heating mechanisms prevail near or within the auroral oval; therefore, the ion upflow occurrence rate observed by PFISR strongly depends on its relative location to the auroral oval, the strength of auroral precipitation, and the convection flow speed.

As shown in section 3.1, there is a strong day-night asymmetry of the upflow occurrence frequency with clear preference for nightside. This agrees well with previous statistical studies done by Keating et al. (1990) and Foster et al. (1998) using data from EISCAT at Tromsø (~ 66.7 MLat, similar to PFISR at ~ 65.5 MLat) from 1984 to 1996, in which they found a peak of upflow occurrence frequency near 23 MLT varying from 12% to 30% as the solar cycle shifts from minimum to maximum. In this study, the period selected is the first part of the solar maximum during solar cycle 24, which was comparable to the period 1987–1989. However, in this study, the peak of upflow occurrence rate, that is, $\sim 12\%$ near 0 MLT, is lower than their results during 1987–1989 with a peak of upflow occurrence $\sim 20\%$ near 23 MLT. This is due to the fact that solar cycle 24 is much weaker than solar cycle 22.

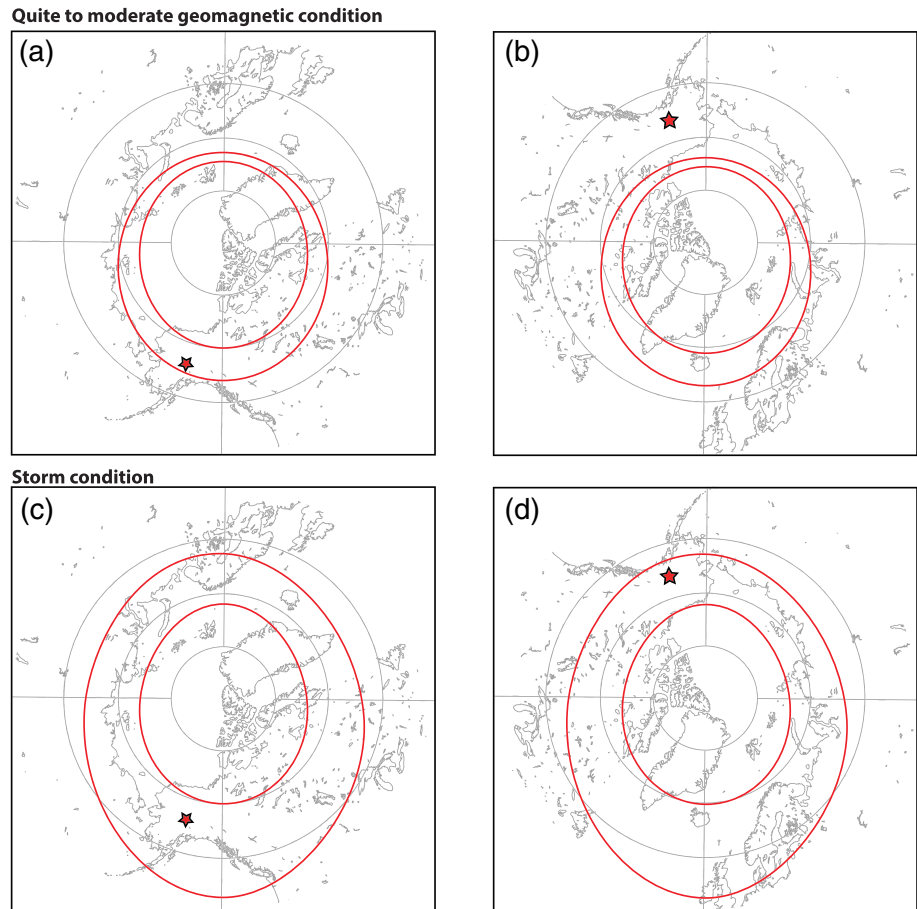


Figure 15. Illustration of PFISR location, marked by the star, relative to the auroral zone, during (a, b) quiet to moderate geomagnetic condition and (c, d) storm condition.

This day-night asymmetry can be understood by the relative location of PFISR to auroral oval. As illustrated in Figures 15a and 15b, under quiet and moderate geomagnetic conditions, this latitude is usually several degrees equatorward of the auroral oval on the dayside but within the nightside auroral oval. During strong driving conditions (Figures 15c and 15d), such as geomagnetic storms, the auroral oval expands equatorward both on the dayside and nightside, and it could extend to the PFISR latitude or even beyond. The ion upflow occurrence rate starts to show a positive correlation with the geomagnetic activity levels under these circumstances, for example, when the AE index exceeds 1,000 nT (Figure 7b) or the SymH index reaches -120 nT (Figure 8b).

The absence of correlation between dayside upflow occurrence and the solar wind and IMF parameters indicates the limited effects from these individual parameters on regions at latitudes as low as PFISR. While in the nightside auroral zone, where parameters like the solar wind velocity, dynamic pressure, and the IMF B_z have direct influence on the precipitation intensity and convection velocity, such correlations are much stronger. This result suggests that the nightside auroral oval is a key region for supplying ions into the magnetosphere.

Compared to the study using data from the EISCAT Svalbard radar (ESR) located at 75.2 MLat (Liu et al., 2001; Ogawa et al., 2009), a clear difference in the diurnal distribution of ion upflow occurrence rate is found. Data from ESR revealed that ion upflow occurs most frequently on the dayside (09–15 MLT), while PFISR observed much higher frequency for ion upflow on the nightside (21–03 MLT). Due to the difference in geomagnetic latitude, ESR is closer/at auroral zone on the dayside while PFISR is closer/at auroral zone on the nightside. Combining results from both studies, we can conclude that ion upflow occurs preferentially at the dayside cusp and nightside auroral zone.

The altitude distribution shown in Figure 3 suggests that on the nightside ion upflow tends to occur at ~400 km, nearly 100 km lower than that on the dayside. This is consistent with the result reported by Ogawa et al. (2009), which showed that upflow observed during nighttime tends to occur more often at lower altitudes ~200 km than those during daytime. The main factor contributing to this altitude difference is likely the ionosphere scale height decreasing from the dayside to the nightside due to diurnal variation of solar radiation and therefore plasma temperature, as shown in Figures 5a and 5b. Another potential reason is that in the nightside auroral oval energetic particle precipitation can penetrate to the *E* region or even below, while near the dayside cusp region soft particle precipitations are often observed to cause electron heating over a wide range of altitudes above 300 km, accelerating the ions upward through ambipolar electric field (e.g., Burchill et al., 2010).

As shown in Figures 4a–4c, the enhanced plasma density, ion, and electron temperature associated with the ion upflow between 15–6 MLT indicate contributions from both frictional heatings and particle precipitation. However, on the dayside between 7 and 14 MLT, no significant difference are seen in the density or temperature distribution of the ion upflow observed. Ogawa et al. (2009) suggested that 15–50% of the upflow they found at some MLTs without any ion or electron temperature increase were probably because the time scale of precipitations or Joule heating, in comparison with the time scale of the ion upflow, might be too short for them to be observed simultaneously with the upflow by the ISR. Simulation results by Cohen et al. (2015) suggest that the high plasma number density on the dayside would result in less significant temperature change when given a certain amount of precipitation energy input, but the resulting flux can still increase, as shown in Figure 4d, since more ions are being accelerated.

4.2. Downflow

Ion downflow has been observed within the tongue-of-ionization and polar cap patches (Ren et al., 2018) or within the SED plume (Zou et al., 2014), which are typical density structures in the high-latitude ionosphere during geomagnetic disturbed periods (Crowley, 1996; Deng & Ridley, 2006; Foster, 1993; Foster et al., 2005; Heelis et al., 2009; Hosokawa et al., 2010; Moen et al., 2008; Ren et al., 2020; Sato & Rourke, 1964; Thomas et al., 2013; Wang et al., 2019; Weber et al., 1984; Zhang et al., 2015; Zou & Ridley, 2016). In addition, Y. Shen et al. (2018) showed that downflow associated with ion heating and broadband extremely low frequency (BBELF) waves can occur at altitudes as low as 350–450 km and often in the postmidnight to dawn sector. This could be a potential mechanism producing the downflow observed near 2–6 MLT and ~450 km altitude in our study, which are associated with clear ion temperature increase as shown in Figure 5a. Future study is required to identify potential conjugate events with simultaneous satellite and PFISR conjunctions.

The preference of the ion downflow during strong positive B_y and southward B_z at the auroral latitudes has never been reported before. It has been well known that IMF B_y sign change could introduce asymmetries in the ionospheric convection and thermospheric wind pattern (e.g., Walsh et al., 2014, and references therein). In Zou et al. (2013, 2014) and Zou and Ridley (2016), large ion downflow has been observed both by PFISR and in the numerical simulation to be associated with the storm-enhanced density (SED) base and SED plume. In these studies, they found that the downflow was due to a combination of enhanced poleward thermospheric wind and enhanced pressure gradient force within the plume. We have compared the clustered downflow events (more than 50 events within 6 hr) in our data set with the events presented in Zou et al. (2014) and indeed found that they tend to occur on the dayside within SEDs, such as the 13–14 October 2011, 13–14 November 2012, and 23–24 April 2012 storms shown in Figure 6 in Zou et al. (2014). The association with the SED can also explain the clear positive correlation between downflow occurrence and geomagnetic activity levels (Figures 7e and 8e) only on the dayside, because the SED is only present during storm time on the dayside subauroral region and its size and strength could be positively correlated with the storm intensity. Figure 2 clearly shows that the downward flows tend to occur more often in the afternoon sector. This is also likely due to the fact that the SED and SED plume are strongest in the afternoon sector.

5. Summary and Conclusions

Using the Poker Flat Incoherent Scatter Radar (PFISR), located near Fairbanks, Alaska, the dependences of ion upflow and downflow in the ionosphere in terms of the geomagnetic activity and solar wind and IMF conditions have been investigated. Here is the summary for the our findings:

1. Ion upflow over PFISR are twice more likely to occur on the nightside than that on the dayside and occurs slightly more often near summer solstice during May, June, and July.
2. On the nightside, both upflow and downflow tend to occur around 400 km, while on the dayside the altitude increases to slightly above/below 500 km for upflow/downflow.
3. Electron temperature and density enhancement for upflow are observed from 16 MLT to 6 MLT throughout the night side, suggesting the association with auroral particle precipitations. Median ion temperature increase as large as 100 K are seen from 16 MLT to 6 MLT as well, suggesting contributions from enhanced convection flow speed and frictional heatings.
4. The occurrence frequency of both upflow and downflow increases almost monotonically as convection velocity increases. The frequency grows more rapidly on the nightside.
5. The occurrence frequency of ion upflow averaged over all MLTs increases with enhanced geomagnetic activity levels represented by the AE and SymH indices. The strongest increasing trend is observed on the nightside with ~30% peak occurrence rate when AE reaches ~1,200 nT and SymH reaches ~-90 nT.
6. On the nightside, the occurrence frequency of ion upflow increases from below 10% with nearly no magnetic perturbation to above 25%, when there is strong southwestward magnetic perturbation reaching magnitude over 400 nT. This southwestward magnetic perturbation is due to a tilted westward electrojet typically seen just poleward of the Harang reversal and thus suggests the nightside upflow tends to occur during periods with clear Harang signatures, such as substorms.
7. Overall, the occurrence rate of ion upflow increases with enhanced solar wind velocity, number density and dynamic pressure, especially on the nightside. In particular, a stronger dependency is identified for fast solar winds (>600 km/s).
8. The occurrence frequency of ion upflow increases as the total IMF and the magnitude of the three IMF components increase. The strongest correlation is observed for southward IMF B_z on the nightside.
9. No clear correlation of upflow on the dayside with any of the solar wind and IMF parameters has been observed. This is because PFISR is typically located equatorward of the dayside auroral zone. Enhanced upflow occurrence on the dayside is observed only during strong geomagnetic activity levels, that is, when SymH reaches -120 nT or AE exceeds 1,000 nT.
10. Ion downflow clearly prefers to occur in the afternoon sector and occur slightly more often near summer solstice.
11. Ion downflow tends to occur more frequently on the dayside during strong geomagnetic activities, indicated by larger AE and more negative SymH, suggesting its association with SED in the dayside subauroral regions.
12. In general, no strong correlation observed between the ion downflow and solar wind parameters, except that when proton number density exceeds over 50 m^{-3} the downflow occurrence frequency increases up to ~18%. The downflow occurrence frequency also slightly increases on the dayside when the solar wind velocity increases.
13. The overall occurrence rate of downflow is not clearly correlated with IMF B_x . However, on the dayside, it clearly occurs much more often when IMF B_y is strongly positive, that is, >10 nT, and when IMF B_z is strongly negative, that is, < -10 nT. Some of these downflow events are associated with SED base and SED plume, as have been shown in Zou et al. (2014).

Acknowledgments

J. Ren and S. Zou acknowledge the National Science Foundation AGS1400998, NASA 80NSSC20K1313, NASA 80NSSC20K0190, and NASA 80NSSC20K0600. J. Lu acknowledges the support from the Undergraduate Research Opportunity Program (UROP) and Undergraduate Research Scholar programs at the University of Michigan. This material is based upon work supported by the Poker Flat Incoherent Scatter Radar which is a major facility funded by the National Science Foundation through cooperative agreement AGS-1840962 to SRI International.

Data Availability Statement

The PFISR data are available at the SRI AMISR database (<https://data.amisr.com/database/61/>) and the Madrigal CEDAR database (<http://cedar.openmadrigal.org/>). Magnetometers at Polar Flat and College are managed by University of Alaska Geophysical Institute, and the data are retrieved through the SuperMAG website (<http://supermag.jhuapl.edu/>, PI Jesper Gjerloev). We acknowledge use of NASA/GSFC's Space Physics Data Facility's OMNIWeb service, and OMNI data (<https://omniweb.gsfc.nasa.gov/>).

References

- Bates, H. F. (1974). Atmospheric expansion from Joule heating. *Planetary and Space Science*, 22(6), 925–937. [https://doi.org/10.1016/0032-0633\(74\)90162-7](https://doi.org/10.1016/0032-0633(74)90162-7)
- Browett, S. D., Fear, R. C., Grocott, A., & Milan, S. E. (2017). Timescales for the penetration of IMF B_y into the Earth's magnetotail. *Journal of Geophysical Research: Space Physics*, 122(1), 579–593. <https://doi.org/10.1002/2016JA023198>
- Buchert, S. C., Ogawa, Y., Fujii, R., & van Eyken, A. P. (2004). Observations of diverging field-aligned ion flow with the ESR. *Annales Geophysicae*, 22(3), 889–899. <https://doi.org/10.5194/angeo-22-889-2004>

- Burchill, J. K., Knudsen, D. J., Clemmons, J. H., Oksavik, K., Pfaff, R. F., Steigies, C. T., et al. (2010). Thermal ion upflow in the cusp ionosphere and its dependence on soft electron energy flux. *Journal of Geophysical Research: Space Physics*, *115*, A05206. <https://doi.org/10.1029/2009JA015006>
- Chappell, C. R. (2015). The role of the ionosphere in providing plasma to the terrestrial magnetosphere—An historical overview. *Space Science Reviews*, *192*(1–4), 5–25. <https://doi.org/10.1007/s11214-015-0168-5>
- Cohen, I. J., Lessard, M. R., Varney, R. H., Oksavik, K., Zettergren, M., & Lynch, K. A. (2015). Ion upflow dependence on ionospheric density and solar photoionization. *Journal of Geophysical Research: Space Physics*, 39–52. <https://doi.org/10.1002/2015JA021523>
- Coley, W. R., Heelis, R. A., & Hairston, M. R. (2006). Characteristics of high-latitude vertical plasma flow from the Defense Meteorological Satellite Program. *Journal of Geophysical Research*, *111*, A11314. <https://doi.org/10.1029/2005JA011553>
- Crowley, G. (1996). Critical review of ionospheric patches and blobs. In W. R. Stone (Ed.), *Review of radio science, 1993–1996* (pp. 619–648). New York: Oxford University Press.
- Deng, Y., & Ridley, A. J. (2006). Role of vertical ion convection in the high-latitude ionospheric plasma distribution. *Journal of Geophysical Research*, *111*, A09314. <https://doi.org/10.1029/2006JA011637>
- Endo, M., Fujii, R., Ogawa, Y., Buchert, S. C., Nozawa, S., Watanabe, S., & Yoshida, N. (1999). Ion upflow and downflow at the topside ionosphere observed by the EISCAT VHF radar. *Annales Geophysicae*, *18*, 170–181. <https://doi.org/10.1007/s00585-000-0170-3>
- Foster, C., Lester, M., & Davies, J. A. (1998). A statistical study of diurnal, seasonal and solar cycle variations of *F*-region and topside auroral upflows observed by EISCAT between 1984 and 1996. *Annales Geophysicae*, *16*, 1144–1158. <https://doi.org/10.1007/s00585-998-1144-0>
- Foster, J. C. (1993). Storm time plasma transport at middle and high latitudes. *Journal of Geophysical Research*, *98*(A2), 1675–1689. <https://doi.org/10.1029/92JA02032>
- Foster, J. C., Coster, A. J., Erickson, P. J., Holt, J. M., Lind, F. D., Rideout, W., et al. (2005). Multiradar observations of the polar tongue of ionization. *Journal of Geophysical Research*, *110*, A09S31. <https://doi.org/10.1029/2004JA010928>
- Gjerloev, J. W. (2012). The SuperMAG data processing technique. *Journal of Geophysical Research: Space Physics*, *117*, A09213. <https://doi.org/10.1029/2012JA017683>
- Heelis, R. A., Sojka, J. J., David, M., & Schunk, R. W. (2009). Storm time density enhancements in the middle-latitude dayside ionosphere. *Journal of Geophysical Research*, *114*, A03315. <https://doi.org/10.1029/2008JA013690>
- Hosokawa, K., Tsugawa, T., Shiokawa, K., Otsuka, Y., Nishitani, N., Ogawa, T., & Hairston, M. R. (2010). Dynamic temporal evolution of polar cap tongue of ionization during magnetic storm. *Journal of Geophysical Research*, *115*, A12333. <https://doi.org/10.1029/2010JA015848>
- Ji, E. Y., Jee, G., & Lee, C. (2019). Characteristics of the occurrence of ion upflow in association with ion/electron heating in the polar ionosphere. *Journal of Geophysical Research: Space Physics*, *124*, 6226–6236. <https://doi.org/10.1029/2019JA026799>
- Keating, J. G., Mulligan, F. J., Doyle, D. B., Winsor, K. J., & Lockwood, M. (1990). A statistical study of large field-aligned flows of thermal ions at high-latitudes. *Planetary and Space Science*, *38*(9), 1187–1201. [https://doi.org/10.1016/0032-0633\(90\)90026-M](https://doi.org/10.1016/0032-0633(90)90026-M)
- Liu, H., Ma, S.-Y., & Schlegel, K. (2001). Diurnal, seasonal, and geomagnetic variations of large fieldaligned ion upflows in the high-latitude ionospheric *F* region. *Journal of Geophysical Research*, *106*(A11), 24,651–24,661. <https://doi.org/10.1029/2001JA900047>
- Loranc, M., Hanson, W. B., Heelis, R. A., & St-Maurice, J.-P. (1991). A morphological study of vertical ionospheric flows in the high-latitude *F* region. *Journal of Geophysical Research*, *96*(A3), 3627. <https://doi.org/10.1029/90JA02242>
- Loranc, M., & St-Maurice, J.-P. (1994). A time-dependent gyro-kinetic model of thermal ion upflows in the high-latitude *F* region. *Journal of Geophysical Research*, *99*(A9), 17429. <https://doi.org/10.1029/93JA01852>
- Lotko, W. (2007). The magnetosphere–ionosphere system from the perspective of plasma circulation: A tutorial. *Journal of Atmospheric and Solar-Terrestrial Physics*, *69*(3), 191–211. <https://doi.org/10.1016/j.jastp.2006.08.011>
- Ma, Y. Z., Zhang, Q. H., Xing, Z. Y., Jayachandran, P. T., Moen, J., Heelis, R. A., & Wang, Y. (2018). Combined contribution of solar illumination, solar activity, and convection to ion upflow above the polar cap. *Journal of Geophysical Research: Space Physics*, *123*, 4317–4328. <https://doi.org/10.1029/2017JA024974>
- Moen, J., Qiu, X. C., Carlson, H. C., Fujii, R., & McCrea, I. W. (2008). On the diurnal variability in *F2*-region plasma density above the EISCAT Svalbard radar. *Annales de Geophysique*, *26*(8), 2427–2433. <https://doi.org/10.5194/angeo-26-2427-2008>
- Moore, T. E., & Horwitz, J. L. (2007). Stellar ablation of planetary atmospheres. *Reviews of Geophysics*, *45*, RG3002. <https://doi.org/10.1029/2005RG000194>
- Nilsson, H., Waara, M., Marghitu, O., Yamauchi, M., Lundin, R., Rème, H., et al. (2008). Transients in oxygen outflow above the polar cap as observed by the cluster spacecraft. *Annales Geophysicae*, *26*(11), 3365–3373. <https://doi.org/10.5194/angeo-26-3365-2008>
- Ogawa, Y., Buchert, S. C., Fujii, R., Nozawa, S., & van Eyken, A. P. (2009). Characteristics of ion upflow and downflow observed with the European Incoherent Scatter Svalbard Radar. *Journal of Geophysical Research: Space Physics*, *114*(A5), A05305. <https://doi.org/10.1029/2008JA013817>
- Ogawa, Y., Seki, K., Keika, K., & Ebihara, Y. (2019). Characteristics of CME- and CIR-driven ion upflows in the polar ionosphere. *Journal of Geophysical Research: Space Physics*, *124*, 3637–3649. <https://doi.org/10.1029/2018JA025870>
- Redmon, R. J., Peterson, W. K., Andersson, L., Kihn, E. A., Denig, W. F., Hairston, M., & Coley, R. (2010). Vertical thermal O⁺ flows at 850 km in dynamic auroral boundary coordinates. *Journal of Geophysical Research: Space Physics*, *115*, A00J08. <https://doi.org/10.1029/2010JA015589>
- Ren, J., Zou, S., Gillies, R. G., Donovan, E., & Varney, R. H. (2018). Statistical characteristics of polar cap patches observed by RISR-C. *Journal of Geophysical Research: Space Physics*, *123*, 6981–6995. <https://doi.org/10.1029/2018JA025621>
- Ren, J., Zou, S., Kendall, E., Coster, A., Sterne, K., & Ruohoniemi, M. (2020). Direct observations of a polar cap patch formation associated with dayside reconnection driven fast flow. *Journal of Geophysical Research: Space Physics*, *125*, e2019JA027745. <https://doi.org/10.1029/2019JA027745>
- Rong, Z. J., Lui, A. T. Y., Wan, W. X., Yang, Y. Y., Shen, C., Petrukovich, A. A., et al. (2015). Time delay of interplanetary magnetic field penetration into Earth's magnetotail. *Journal of Geophysical Research: Space Physics*, *120*, 3406–3414. <https://doi.org/10.1002/2014JA020452>
- Sato, T., & Rourke, G. F. (1964). *F*-region enhancements in the Antarctic. *Journal of Geophysical Research*, *69*(21), 4591–4607. <https://doi.org/10.1029/jz069i021p04591>
- Semeter, J., Heinselman, C. J., Thayer, J. P., Doe, R. A., & Frey, H. U. (2003). Ion upflow enhanced by drifting *F*-region plasma structure along the nightside polar cap boundary. *Geophysical Research Letters*, *30*(22), 2139. <https://doi.org/10.1029/2003gl017747>
- Seo, Y., Horwitz, J. L., & Caton, R. (1997). Statistical relationships between high-latitude ionospheric *F* region/topside upflows and their drivers: DE 2 observations. *Journal of Geophysical Research*, *102*(A4), 7493–7500. <https://doi.org/10.1029/97JA00151>

- Shen, Y., Knudsen, D. J., Burchill, J. K., Howarth, A. D., Yau, A. W., Miles, D. M., et al. (2018). Low-altitude ion heating, downflowing ions, and BBELF waves in the return current region. *Journal of Geophysical Research: Space Physics*, *123*, 3087–3110. <https://doi.org/10.1002/2017JA024955>
- Strangeway, R. J. (2005). Factors controlling ionospheric outflows as observed at intermediate altitudes. *Journal of Geophysical Research*, *110*, A03221. <https://doi.org/10.1029/2004JA010829>
- Thomas, E. G., Baker, J. B. H., Ruohoniemi, J. M., Clausen, L. B. N., Coster, A. J., Foster, J. C., & Erickson, P. J. (2013). Direct observations of the role of convection electric field in the formation of a polar tongue of ionization from storm enhanced density. *Journal of Geophysical Research: Space Physics*, *118*, 1180–1189. <https://doi.org/10.1002/jgra.50116>
- Tu, J.-N., Dhar, M., Song, P., Reinisch, B. W., Green, J. L., Benson, R. F., & Coster, A. J. (2007). Extreme polar cap density enhancements along magnetic field lines during an intense geomagnetic storm. *Journal of Geophysical Research*, *112*, A05201. <https://doi.org/10.1029/2006JA012034>
- Wahlund, J. -E., Opgenoorth, H. J., Häggström, I., Winsor, K. J., & Jones, G. O. L. (1992). EISCAT observations of topside ionospheric ion outflows during auroral activity: Revisited. *Journal of Geophysical Research: Space Physics*, *97*(A3), 3019–3037. <https://doi.org/10.1029/91ja02438>
- Walsh, A. P., Haaland, S., Forsyth, C., Keesee, A. M., Kissinger, J., Li, K., et al. (2014). Dawn–dusk asymmetries in the coupled solar wind–magnetosphere–ionosphere system: A review. *Annales Geophysicae*, *32*(7), 705–737. <https://doi.org/10.5194/angeo-32-705-2014>
- Wang, Z., Zou, S., Coppeans, T., Ren, J., Ridley, A., & Gombosi, T. (2019). Segmentation of SED by boundary flows associated with westward drifting partial ring current. *Geophysical Research Letters*, *46*, 7920–7928. <https://doi.org/10.1029/2019GL084041>
- Weber, E. J., Buchau, J., Moore, J. G., Sharber, J. R., Livingston, R. C., Winningham, J. D., & Reinisch, B. W. (1984). F layer ionization patches in the polar cap. *Journal of Geophysical Research*, *89*(A3), 1683–1694. <https://doi.org/10.1029/JA089iA03p01683>
- Welling, D. T., Andre, M., Dandouras, I., Delcourt, D., Fazakerley, A., Dontaine, D., et al. (2015). The Earth: Plasma sources, losses, and transport processes. *Space Science Reviews*, *192*(1–4), 145–208. <https://doi.org/10.1007/s11214-015-0187-2>
- Wu, X.-Y., Horwitz, J. L., & Seo, Y. (2000). Statistical analysis of F region and topside ionospheric ion field-aligned flows at high latitudes. *Journal of Geophysical Research*, *105*(A2), 2477–2494. <https://doi.org/10.1029/1999JA900437>
- Yau, A. W., & André, M. (1997). Sources of ion outflow in the high latitude ionosphere. *Space Science Reviews*, *80*, 1–25. <https://doi.org/10.1023/A:1004947203046>
- Zhang, Q. H., Lockwood, M., Foster, J. C., Zhang, S. R., Zhang, B. C., McCrea, I. W., et al. (2015). Direct observations of the full Dungey convection cycle in the polar ionosphere for southward interplanetary magnetic field conditions. *Journal of Geophysical Research Space Physics*, *120*, 4519–4530. <https://doi.org/10.1002/2015JA021172>
- Zhang, Q.-H., Zong, Q., Lockwood, M., Heelis, R. A., Hairston, M., Liang, J., et al. (2016). Earth's ion upflow associated with polar cap patches: Global and in situ observations. *Geophysical Research Letters*, *43*, 1845–1853. <https://doi.org/10.1002/2016GL067897>
- Zou, S., Lyons, L. R., Nicolls, M. J., Heinselman, C. J., & Mende, S. B. (2009). Nightside ionospheric electrodynamics associated with substorms: PFISR and THEMIS ASI observations. *Journal of Geophysical Research: Space Physics*, *114*, A12301. <https://doi.org/10.1029/2009JA014259>
- Zou, S., Lyons, L. R., Wang, C.-P., Boudouridis, A., Ruohoniemi, J. M., Anderson, P. C., et al. (2009). On the coupling between the Harang reversal evolution and substorm dynamics: A synthesis of SuperDARN, DMSP and IMAGE observations. *Journal of Geophysical Research*, *114*, A01205. <https://doi.org/10.1029/2008JA013449>
- Zou, S., Moldwin, M. B., Ridley, A. J., Nicolls, M. J., Coster, A. J., Thomas, E. G., & Ruohoniemi, J. M. (2014). On the generation/decay of the storm-enhanced density (SED) plumes: Role of the convection flow and field-aligned ion flow. *Journal of Geophysical Research*, *119*, 8543–8559. <https://doi.org/10.1002/2014JA020408>
- Zou, S., Ozturk, D., Varney, R., & Reimer, A. (2017). Effects of sudden commencement on the ionosphere: PFISR observations and global MHD simulation. *Geophysical Research Letters*, *44*, 3047–3058. <https://doi.org/10.1002/2017GL072678>
- Zou, S., Ridley, A., Jia, X., Boyd, E., Nicolls, M., Coster, A., et al. (2017). PFISR observation of intense ion upflow fluxes associated with an SED during the 1 June 2013 geomagnetic storm. *Journal of Geophysical Research: Space Physics*, *122*, 2589–2604. <https://doi.org/10.1002/2016JA023697>
- Zou, S., & Ridley, A. J. (2016). Modeling of the evolution of storm-enhanced density (SED) plume during the Oct. 24–25, 2011 geomagnetic storm. In C. R. Chappell, R. W. Schunk, P. M. Banks, J. L. Burch, R. M. Thorne (Eds.), *Magnetosphere-ionosphere coupling in the solar system, Geophysical Monograph Series* (Vol. 222, pp. 205–213). Hoboken, NJ, USA: John Wiley & Sons, Inc. <https://doi.org/10.1002/9781119066880.ch16>
- Zou, S., Ridley, A. J., Moldwin, M. B., Nicolls, M. J., Coster, A. J., Thomas, E. G., & Ruohoniemi, J. M. (2013). Multi-instrument observations of SED during 24–25 October 2011 storm: Implications for SED formation processes. *Journal of Geophysical Research*, *118*, 7798–7809. <https://doi.org/10.1002/2013JA018860>